Adaptive multigrid solutions of gravity-driven thin liquid films over topography

Y.C. Lee, H.M. Thompson and P.H. Gaskell *

School of Mechanical Engineering, The University of Leeds, Leeds LS2 9JT, UK.

Abstract

Gravity-driven continuous thin film flow over a plane, containing well-defined single and grouped topographic features, is modelled as a Stokes flow using lubrication theory. The associated time dependent, nonlinear, coupled set of governing equations are solved using a Full Approximation Storage (FAS) Multigrid algorithm by employing automatic mesh adaptivity, the power, efficiency and accuracy of which is demonstrated by comparing the results with corresponding global fine-mesh solutions. These show that automatic grid refinement effectively restricts the use of fine grids to regions of rapid flow development which, for flow over the topographies considered, includes the topography itself, the upstream Capillary ridge, downstream surge region, and the characteristic bow wave. It is shown that for the accurate solution of such flow problems, adapative Multigridding offers increased flexibility together with a significant reduction in memory requirement. This is further demonstrated by solving the problem of transient flow over a trench topography, generated by a sinusoidally varying inlet condition.

Key words: adaptivity, Multigrid, topography, thin film

1 Introduction

The behaviour of continuous thin liquid films which flow over non-porous substrates is of enormous significance in a wide variety of biological, engineering and industrial applications. Although much is now known about such flow over homogeneous surfaces [1], the inherently more challenging problem of flow over surfaces containing topography has received far less attention. The latter is encountered in many biological processes including, for example, when the liquid lining in the lung redistributes following the impact of an inhaled particle [2], when tear films coat the curved cornea in the eye [3], or in membrane blood oxygenators in extra-corporeal systems [4]. They are also encountered widely in manufacturing industry, particularly in the electronics sector (displays, printed circuits, micro-devices, sensors etc) whose processes usually involve the successive deposition of several thin liquid layers over uneven substrates combined with photolithography at each stage [5].

Increasing demands viz. function, quality and finish are driving the requirement for a better understanding of the mechanisms leading to free surface non-uniformities, and significantly how to control defects caused when a film encounters a topographical heterogeneity. A major goal is, not surprisingly, the minimisation of free surface deviations from planarity, for either functional or aesthetic reasons, or both. This represents an extremely challenging practical problem since free surface disturbances caused by even small-scale topography can persist over length scales several orders of magnitude greater than the actual size of the topography.

* Corresponding author. Tel. :+44 (0)113 343 2201. Fax:+44 (0)113 232 4611
Email address: p.h.gaskell@leeds.ac.uk (P.H. Gaskell).

Until quite recently, attention has focussed on thin film formation over simple, step topographies, modelled in terms of the long-wave, lubrication approximation [6]. Kalliadasis & Homsy [7], for example, considered the flow over a one-dimensional trench under the action of an external body force, before moving on to investigate the stability of Capillary ridges in flow over a step-down topography [8]. Thin film flow over one-dimensional sinusoidal topography has also been considered in a recent series of experimental [9,10], analytical [11] and numerical investigations [12]; these have highlighted the rich variety of flow structure, eddy generation and mass transfer phenomena that can be produced by even simple topography shapes.

Due to the formidable experimental, theoretical and computational challenges involved, fully three-dimensional flow over topography has received far less attention. Indeed, the important early contribution of Pozrikidis & Thoroddsen [13], which showed that even a small particle topography can result in significant upstream and downstream disturbances to the free surface of the film, remained the main contribution in the area until Hayes, O'Brien & Lammers [14] formulated a Green's function approximation to solve for flow over small topographies of arbitrary shape. Bielarz & Kalliadasis [15] subsequently considered flow over larger, three-dimensional mounds. They employed a lubrication model for the flow and used a semi-implicit time-spliting technique, see for example [16], together with the popular alternating-direction implicit (ADI) scheme, to solve the resulting governing 4th-order partial differential equation. Their numerical approach follows that of Schwartz & Eley [17], who used a lubrication framework to investigate droplet spreading phenomena. Their motivation for using this method of solution is that it combines some of the stability properties of implicit schemes with the cost efficienty of explicit

ones. This has been explored by Daniels et al [18] who, considering the flow of a droplet down an inclined plane, showed that a fully implicit multigrid lubrication flow solver is more robust, returns an order of magnitude improvement in the rate of convergence for the levels of grid refinement required for accuracy and requires far less memory. Gaskell et al [19] demonstrated the point still further by solving a series of problems involving the motion of droplets on chemically and topographically heterogeneous surfaces by combining a multigrid solver with adaptive time-stepping [20].

As to the appropriateness of the lubrication approximation for solving the problem of the flow of continous thin films over localised well-defined topography, the full numerical solution of the corresponding Stokes problem using boundary elements [21] and Navier-Stokes equations, using finite elements [22], have demonstrated that it is suprisingly accurate even in regions of parameter space where it is not strictly valid. This is reinforced by the fact that the numerical predictions are found to agree very well indeed with the corresponding experimental data of Decre & Baret [5], in that they predict and capture accurately the characteristic horseshoe *bow wave* generated downstream of a localised topography. Similarly, a lubrication model has been used recently to solve the three-dimensional flow of evaporating thin films over topography [23]; the use of fine meshes revealing that evaporation can lead to persistent heterogeneities in the composition of the resin/solvent mixture which have the potential to cause unacceptable variations in dry, functional coatings.

Despite a Multigrid approach being an effective means of solving thin film flows, the use of uniformly-spaced fine grids is unnecessarily inefficient for practical problems of the type considered here since topographic heterogeneities are often either very localised and sparsely spread across the substrate or, as is

shown, can be grouped together in a specific pattern to minimise free-surface deformations. The key thrust of the present work, therefore, is to formulate and utilise an efficient and accurate automatic, adaptive local grid refinement strategy, which constrains the use of fine grids to regions of the solution domain where they are required, i.e. in the vicinity of the topographies themselves, thus allowing much coarser grids to be employed over the rest of the solution domain.

The idea of local mesh refinement is not new. Indeed, numerical investigations using mesh adaptivity to balance local discretisation errors based on the nature of the problem being investigated have been performed for a wide range of applications. Specifying the adaptive regions a-priori, Bai and Brandt [24] applied patial refinements to Poisson's equation in two-dimensions and showed that accurate solutions are preserved by retaining conservation forms where local refinements are introduced [25]. Thompson and Ferziger [26] used this idea to develop an efficient and accurate adaptive Multigrid approach for cavity driven flows. Patch-based adaptive mesh refinement (AMR) techniques [27] have since become very popular for spatial discretisation by using a dynamic sequence of overlapping grids of increasing fineness from the underlying coarse grid. These have been used in a host of scientific simulations ranging, for example, from turbulent flows [28], porous media investigations [29] and elastohydrodynamic lubrication problems [30] to a range of bio-medical problems [31]. The alternative approach of applying adaptive h-refinement has also proven popular and particularly beneficial when solving Partial Differential Equations (PDEs) with singular characteristics [24], non-linearities [27], or rapidly changing properties [32].

Section 2 describes the flows under consideration together with the governing

lubrication model. The Multigrid approach and automatic grid refinement strategy are presented in Section 3, followed by numerical results in section 4. The conclusions of section 5 highlight the benefits of using a fully implicit, Multigrid algorithm with automatic adaptive mesh refinement for the efficient solution of this important class of fluid flow problems.

2 Problem Specification and Mathematical Formulation

Figure 1 shows a sketch of the motion of a thin liquid film of thickness $H(X,Y)$ over a flat substrate, containing three topographic trenches of various cross-sectional shapes, inclined at an angle θ to the horizontal, with a constant volumetric flow Q_0 per unit width. The liquid is assumed Newtonian and incompressible, with constant density ρ, viscosity μ and surface tension σ, and its motion governed by the Navier-Stokes and continuity equations, viz:

$$\rho\left(\frac{\partial \underline{U}}{\partial T} + \underline{U}.\nabla\underline{U}\right) = \; -\nabla P \; + \mu \; \nabla^2\underline{U} \; + \rho \; \underline{g}, \tag{1}$$

$$\nabla.\underline{U} \; = \; 0, \tag{2}$$

where $\underline{U} = (U,V,W)$ and P are the fluid velocity and pressure respectively, T is time and $\underline{g} = g(\sin\theta, 0, -\cos\theta)$ is the acceleration due to gravity.

Following Aksel [33], an appropriate length scale for non-dimensionalisation purposes is the undisturbed fully developed film thickness:

$$H_0 = \left(\frac{3\mu Q_0}{\rho g \sin\theta}\right)^{1/3}, \tag{3}$$

while the characteristic velocity U_0 is taken to be the corresponding surface velocity of the fully developed film, namely:

$$U_0 = \frac{3Q_0}{2H_0} \ . \tag{4}$$

Implicit in the choice of scales is the assumption that $\theta \neq 0$, i.e. the substrate is never horizontal.

The flow over localised topography is analysed using the long wave, lubrication approximation. The equations to be solved for the film thickness $H(X,Y,T)$ and pressure field $P(X,Y,T)$ are derived from expansions of equation (1) and (2) under the assumption that $\epsilon = H_0/L_0$ is small, where L_0 is the characteristic in-plane length scale, written in terms of the following non-dimensional (lower case) variables:

$$h(x,y,t) = \frac{H(X,Y,T)}{H_0}, \quad s(x,y) = \frac{S(X,Y)}{H_0}, \quad (x,y) = \frac{(X,Y)}{L_0},$$
$$z = \frac{Z}{H_0}, \quad p(x,y,t) = \frac{2P(X,Y,T)}{\rho g L_0 \sin\theta}, \quad (u,v,w) = (\frac{U}{U_0}, \frac{V}{U_0}, \frac{W}{\epsilon U_0}), \quad t = \frac{U_0 T}{L_0},$$

where the surface profile of the substrate is given by the topography function $s(x,y)$, so that the fluid film lies between $z = s$ and $z = h + s$.

Neglecting terms $O(\epsilon^2)$, and imposing the no-slip condition on the substrate, $z = s$, and zero tangential stress at the film surface, $z = h + s$, yields the following lubrication equation for h in terms of the pressure field, p, derived by imposing mass conservation:

$$\frac{\partial h}{\partial t} \ = \ \frac{\partial}{\partial x}\left[\frac{h^3}{3}\left(\frac{\partial p}{\partial x} - 2\right)\right] + \frac{\partial}{\partial y}\left[\frac{h^3}{3}\left(\frac{\partial p}{\partial y}\right)\right] \ . \tag{5}$$

The pressure field throughout the film is given by:

$$p = -\frac{\epsilon^3}{Ca}\nabla^2(h+s) + 2\epsilon(h+s-z)\cot\theta \ , \tag{6}$$

where the pressure datum is set to zero. The z-dependence in equation (6) does not have any influence on the film thickness h since its partial derivatives with respect to x and y are both zero. Choosing the length scale L_0 to be proportional to the capillary length, L_c, that is:

$$L_0 = \beta L_c \quad \text{where} \quad L_c = \left(\frac{\sigma H_0}{3\rho g \sin\theta}\right)^{1/3} = \frac{H_0}{(6Ca)^{\frac{1}{3}}} \ , \tag{7}$$

enables equation (6) to be rewritten as:

$$p = -\frac{6}{\beta^3}\nabla^2(h+s) + \frac{2}{\beta}6^{1/3}N(h+s) \ , \tag{8}$$

in terms of the parameter $N = Ca^{1/3}\cot\theta$, which measures the importance of the normal component of gravity on the flow. If $N \ll 1$ the latter is negligible and (8) becomes parameter free in the sense that the behaviour of the thin film will depend only on the topographic features.

Following previous authors [6], the topographies are defined via arctangent functions which enable the steepness of their sides to be controlled easily. For a topographic peak of rectangular cross-section of length l_t, width w_t and height s_0 centred at (x_t, y_t), for example, the topography function $s(x,y)$ is defined by:

$$s(x,y) = \frac{s_0}{b_0}\left[\tan^{-1}\left(\frac{\beta(x-x_t)-l_t/2)}{\gamma l_t}\right) + \tan^{-1}\left(\frac{\beta(x_t-x)-l_t/2}{\gamma l_t}\right)\right] \times \left[\tan^{-1}\left(\frac{\beta(y-y_t)-w_t/2}{\gamma w_t}\right) + \tan^{-1}\left(\frac{\beta(y_t-y)-w_t/2}{\gamma w_t}\right)\right] \ , \tag{9}$$

where γ is an adjustable parameter which controls the steepness:

$$b_0 \;=\; 4\tan^{-1}\left(\frac{1}{2\gamma}\right)\tan^{-1}\left(\frac{A}{2\gamma}\right), \tag{10}$$

and $A = w_t/l_t$ is the aspect ratio. Similar functions can be derived for other sharp-sided topographies.

The boundary conditions result from the assumptions that the flow is fully developed upstream and downstream, namely:

$$h(x=0,y)=1\ ,\ \frac{\partial h}{\partial x}|_{x=0}=0\ ,\ \frac{\partial h}{\partial x}|_{x=1}=\frac{\partial p}{\partial x}|_{x=1}=0\ , \tag{11}$$

while zero flow at the boundaries in the spanwise directions requires:

$$\frac{\partial p}{\partial y}|_{y=0}=\frac{\partial p}{\partial y}|_{y=1}=\frac{\partial h}{\partial y}|_{y=0}=\frac{\partial h}{\partial y}|_{y=1}=0\ . \tag{12}$$

3 Numerical Method

3.1 Spatial Discretisation

The lubrication equations (5) and (8) are solved on a square computational domain, $(x,y) \in \Omega = (0,1)\times(0,1)$, with uniform grid spacings in the x and y directions, Δ_x and Δ_y, respectively. Although the techniques used here are readily applicable to cases where $\Delta_x \neq \Delta_y$, for simplicity attention is restricted to cases where the spatial mesh size is the same in each direction, i.e. $\Delta_x = \Delta_y = \Delta$, say.

Following Gaskell et al [19], a Finite Difference discretisation is used where control volumes are centred at grid vertices, $\underline{h}$ and $\underline{p}$ are assumed to be piecewise

constant and the flux variables are defined at the control volume boundaries, as indicated by the dashed lines in Figure 2. Equations (5) and (8) can then be approximated spatially using a central-difference scheme [34], leading to the following second-order accurate spatial discretisation:

$$\frac{\partial h_{i,j}}{\partial t} = \frac{1}{\Delta^2}\Big[\frac{h^3}{3}|_{i+\frac{1}{2},j}\,(p_{i+1,j} - p_{i,j}) - \frac{h^3}{3}|_{i-\frac{1}{2},j}\,(p_{i,j} - p_{i-1,j}) + \frac{h^3}{3}|_{i,j+\frac{1}{2}}\,(p_{i,j+1} - p_{i,j}) - \frac{h^3}{3}|_{i,j-\frac{1}{2}}\,(p_{i,j} - p_{i,j-1})\Big] - \frac{2}{\Delta}\Big(\frac{h^3}{3}|_{i+\frac{1}{2},j} - \frac{h^3}{3}|_{i-\frac{1}{2},j}\Big), \tag{13}$$

$$p_{i,j} + \frac{6}{\Delta^2}\Big[(h_{i+1,j} + s_{i+1,j}) + (h_{i-1,j} + s_{i-1,j}) + (h_{i,j+1} + s_{i,j+1}) + (h_{i,j-1} + s_{i,j-1}) - 4(h_{i,j} + s_{i,j})\Big] - 2\sqrt[3]{6}N(h_{i,j} + s_{i,j}) = 0, \tag{14}$$

for each, (i, j), in the computational domain. The terms, $\frac{h^3}{3}|_{i\pm\frac{1}{2},j}$, $\frac{h^3}{3}|_{i,j\pm\frac{1}{2}}$ are the pre-factors obtained from linear interpolation between neighbouring vertices, and given by:

$$\frac{h^3}{3}|_{i+\frac{1}{2},j} = \frac{1}{2}\Big(\frac{1}{3}h^3_{i+1,j} + \frac{1}{3}h^3_{i,j}\Big), \tag{15}$$

with similar expressions for the $\frac{h^3}{3}|_{i-\frac{1}{2},j}$, $\frac{h^3}{3}|_{i,j+\frac{1}{2}}$, and, $\frac{h^3}{3}|_{i,j-\frac{1}{2}}$ terms.

3.2 Temporal Discretisation

The standard implicit, second order accurate Crank-Nicolson method is used to approximate the time-derivatives in equation (13), requiring it to be expressed in differential-algebraic form as:

$$\frac{\partial h_{i,j}}{\partial t} = F(h_{i,j}, p_{i,j}, h_{i\pm1,j}, p_{i\pm1,j}, h_{i,j\pm1}, p_{i,j\pm1}), \tag{16}$$

for each node (i, j) in the computational domain. The implicit nature of the Crank-Nicolson scheme ensures the stability of the time integration. Accordingly, equation (16) is written as an equation for the unknown variables at the end of the $(n+1)$th time step (with superscript $n+1$) at $t = t^{n+1}$ in terms of the known values at the end of the nth time interval, $t = t^n$, via:

$$h_{i,j}^{n+1} - \frac{\Delta t^{n+1}}{2} F(h_{i,j}^{n+1}, p_{i,j}^{n+1}, h_{i\pm1,j}^{n+1}, p_{i\pm1,j}^{n+1}, h_{i,j\pm1}^{n+1}, p_{i,j\pm1}^{n+1})$$
$$= h_{i,j}^{n} - \frac{\Delta t^{n+1}}{2} F(h_{i,j}^{n}, p_{i,j}^{n}, h_{i\pm1,j}^{n}, p_{i\pm1,j}^{n}, h_{i,j\pm1}^{n}, p_{i,j\pm1}^{n}), \qquad (17)$$

for which $\Delta t^{n+1} = t^{n+1} - t^n$, and the right hand sides are given in terms of known values at t^n.

3.3 Multigrid Solution Strategy

A key feature of Multigrid methods is that they offer the prospect of being able to solve a discrete problem with N unknowns in only $O(N)$ operations. Moreover, the intrinsically scalable Multigrid algorithm is readily applicable to both linear and non-linear problems and displays efficiencies that are independent of grid sizes, domain shape and boundary type.

The adaptive Multigrid strategy adopted embodies the Full Approximation Storage (FAS) and Full Multigrid (FMG) concepts introduced by Brandt [35]. The Multigrid uses a sequence of progressingly fine grids, $(\mathcal{G}_k : k = 0, 1, 2, \ldots, K)$, which corresponds to decreasing mesh sizes, $(\Delta_k : k = 0, 1, 2, \ldots, K)$, defined on the domain Ω. On $\mathcal{G}_k$, Δ_k is defined by the number of mesh nodes in each co-ordinate direction, $n_k = 2^{k+c+1} + 1$, where c is a constant defining the resolution of the coarsest grid level. The spatial co-ordinates of its grid points are given by:

$$x_i = (i-1)\Delta_k, \quad y_j = (j-1)\Delta_k \qquad \text{where } \Delta_k = 2^{-(k+c+1)}. \tag{18}$$

By employing a vertex-centered discretisation on uniform quadrilateral grids, the discretised non-linear governing lubrication equations (13) and (14), defined on $\mathcal{G}_k$, may be re-written respectively as:

$$\mathcal{N}_k^h(\underline{h}_k^{n+1}, \underline{p}_k^{n+1}) = \underline{f}_k^h(\underline{h}_k^n, \underline{p}_k^n), \tag{19}$$
$$\mathcal{N}_k^p(\underline{h}_k^{n+1}, \underline{p}_k^{n+1}) = 0, \tag{20}$$

where $\underline{h}_k^n =$ and $\underline{p}_k^n$ are the film thickness and pressures on the kth grid at the nth time step, $t = t^n$, and $\underline{f}_k^h$ corresponds to the right-hand sides of equation (17) on $\mathcal{G}_k$. The Multigrid method can be explained more clearly by expressing equations (19) and (20) via the single equation

$$\mathbf{N}_k \mathbf{u}_k^{n+1} = \mathbf{f}_k(\mathbf{u}_k^n), \tag{21}$$

with $\mathbf{N_k} = (\mathcal{N}_k^h, \mathcal{N}_k^p)$, $\mathbf{u_k} = (\underline{h}_k, \underline{p}_k)^T$ and $\mathbf{f}_k = (f_k^h, f_k^p)$ where $f_k^p = 0$.

3.3.1 The Full Approximation Storage (FAS) Cycle

For reasons of clarity the FAS multigrid algorithm is described first for a sequence of two grid levels with fine grid $\mathcal{G}_1$ and coarse grid $\mathcal{G}_0$. Note that only one Multigrid cycle is used to solve equations (21) but within this cycle a variable number of Multgrid iterations are used, depending on a prescribed error tolerance. Hence, it is necessary to introduce a number, m say, which indicates the present Multigrid iteration. At the beginning of each Multigrid cycle $m = 0$, and increases with the number of Multigrid iterations used.

Starting from a given initial fine grid approximation, $\mathbf{u}_{0_1}^m = (\widetilde{\underline{h}}_{01}^m, \widetilde{\underline{p}}_{01}^m)^T$, the Multigrid process begins by performing a number, ν_1, of pre-relaxation sweeps

on $\mathcal{G}_1$ to yield relaxed fine grid values $\widetilde{\mathbf{u}}_1^m$. This is followed by the coarse grid correction stage where a coarse grid solution on $\mathcal{G}_0$ is computed from the $\widetilde{\mathbf{u}}_1^m$ and its residuals, $\mathbf{d}_1^m = (d_1^{m,h}, d_1^{m,p})^T$, with the use of appropriate inter-grid transfer operators. Once the solution to the coarse grid equations, $\mathbf{w}_0^m = (\underline{w}_0^{m,h}, \underline{w}_0^{m,p})^T$ say, are obtained, the corrections terms, $\mathbf{v}_0^m = (\underline{v}_0^{m,h}, \underline{v}_0^{m,p})^T$, for the fine grid approximation are interpolated back onto $\mathcal{G}_1$. The updated fine grid solution then undergoes ν_2 post-relaxation sweeps to obtain better approximations for the new iterate, $\mathbf{u}_1^{m+1}$, to be used with subsequent Multigrid iterations. This process is repeated until satisfactory convergence is achieved.

The general Multigrid algorithm extends the relaxation and coarse grid correction procedures from a two-grid perspective to include a larger number of grid levels. This allows longer wavelength error modes that are not representable on finer grids to be reduced by relaxation on coarser grid levels. The coarse grid correction scheme is then employed recursively until the discretised equations can either be solved directly or with only a few relaxations. Note that the value of κ, which represents the number of iterations of the Multigrid process at each intermediate grid level, determines the type of coarse grid correction cycle. Here, V-cycles with $\kappa = 1$ are employed. The inter-grid transfer operators used in the Multigrid algorithm consist of restriction operator R_k^{k-1} (from $\mathcal{G}_k$ to $\mathcal{G}_{k-1}$) and prolongation operator, I_{k-1}^k (grid $\mathcal{G}_{k-1}$ to $\mathcal{G}_k$), whose orders depend on the order of derivatives in the PDE being solved [36]. For the second order lubrication equations considered presently, standard half-weighting restriction and bi-linear interpolation are appropriate.

The Full Approximation Storage (FAS) Multigrid algorithm employed can be described using Trottenberg et al's [37] pseudo-code formalism, via:

Multilevel FAS Cycle $\mathbf{u}_{1_k}^{m+1} = \mathrm{MGFASCYC}(k, \mathbf{u}_{0_k}^{m}, \mathbf{f}_k, \nu_1, \nu_2, \kappa)$

(1) Pre-relaxation:

- Perform ν_1 relaxation sweeps:

  $\tilde{\mathbf{u}}_{0_k}^{m} = \mathrm{RELAX}(\mathbf{u}_{0_k}^{m}, \mathbf{f}_k)$

(2) Coarse grid correction:

- Compute residual on $\mathcal{G}_k$

  $\mathbf{d}_k^m = \mathbf{f}_k - \mathbf{N}_k \tilde{\mathbf{u}}_{0_k}^{m}$

- Restrict residual to next coarser grid level on $\mathcal{G}_{k-1}$

  $\mathbf{d}_{k-1}^m = R_k^{k-1} \mathbf{d}_k^m$

- Restrict fine grid solution from $\mathcal{G}_k$

  $\tilde{\mathbf{u}}_{0_{k-1}}^{m} = R_k^{k-1} \tilde{\mathbf{u}}_{0_k}^{m}$

- Compute right hand side on $\mathcal{G}_{k-1}$

  $\mathbf{f}_{k-1} = \mathbf{d}_{k-1}^m + \mathbf{N}_{k-1} \tilde{\mathbf{u}}_{0_{k-1}}^{m}$

- If $k = 1$, solve the problem using the coarse grid solver.

  $\mathbf{N}_{k-1} \mathbf{w}_{k-1}^m = \mathbf{f}_{k-1}$

  If $k > 1$, perform κ iterations using $\tilde{\mathbf{u}}_{0_{k-1}}^{m}$ as initial approximation,

  $\mathbf{w}_{k-1}^m = \mathrm{MGFASCYC}(k-1, \tilde{\mathbf{u}}_{0_{k-1}}^{m}, \mathbf{f}_{k-1}, \nu_1, \nu_2, \kappa)$

- Compute corrections on $\mathcal{G}_{k-1}$ with,

  $\mathbf{v}_{k-1}^m = \mathbf{w}_{k-1}^m - \tilde{\mathbf{u}}_{0_{k-1}}^{m}$

- Interpolate corrections onto $\mathcal{G}_k$

  $\mathbf{v}_k^m = I_{k-1}^k \mathbf{v}_{k-1}^m$

- Update approximated solution on $\mathcal{G}_k$ with,

  $\mathbf{u}_{0_k}^{m} = \tilde{\mathbf{u}}_{0_k}^{m} + \mathbf{v}_k^m$

(3) Post-relaxation:

- Perform ν_2 relaxation sweeps:

  $\mathbf{u}_{1_k}^{m+1} = \mathrm{RELAX}(\mathbf{u}_{0_k}^{m}, \mathbf{f}_k)$

3.3.2 The Full Multigrid (FMG) Cycle

If computations are initiated on the finest grid simply by using an arbitrary initial guess, the Multigrid solution may diverge. This problem can be avoided if the solutions from coarser grids are used to generate an appropriate initial estimate for the next finer grid level in the hierarchy. This is referred to as the Full Multigrid (FMG) technique [38]. The FMG procedure coupled with the FAS algorithm, shown schematically in Figure 3, for a total of 4 grid levels, proceeds as follows. More generally if K is the number of grid levels,

For $k = 0, 1, 2, \ldots, K$

- If $k = 0$, solve $\mathbf{N}_0 \mathbf{u}_0^{m+1} = \mathbf{f}_0$ to obtain initial guess $\mathbf{u}_{1_0}^{m}$
- If $k > 0$,

  Interpolate onto fine grid on $\mathcal{G}_k$

  $\mathbf{u}_{0_k}^{m} = \Pi_{k-1}^{k} \mathbf{u}_{1_{k-1}}^{m}$

  Compute $\mathbf{u}_{1_k}^{m+1} = \mathrm{MGFASCYC}(k, \mathbf{u}_{0_k}^{m}, \mathbf{f}_k, \nu_1, \nu_2, \kappa)$

Note that Π_{k-1}^{k} is a prolongation operator for transferring information from $\mathcal{G}_{k-1}$ to $\mathcal{G}_k$ and its order may or may not be equal to that of the prolongation operator I_{k-1}^{k}.

3.3.3 Relaxation

Error reduction is performed using a fixed number of pre- and post- Red-Black Gauss-Seidel Newton relaxations on equation (21). This requires the local Jacobian to be calculated and yields linearised equations in the form:

$$\frac{\partial \mathcal{N}_k^h}{\partial h_{i,j_k}^{n+1}} \Delta h + \frac{\partial \mathcal{N}_k^h}{\partial p_{i,j_k}^{n+1}} \Delta p = f_k^h - \mathcal{N}_k^h \left(\underline{h}_k^{n+1}, \underline{p}_k^{n+1} \right) \ , \tag{22}$$

$$\frac{\partial \mathcal{N}_k^p}{\partial h_{i,j_k}^{n+1}} \Delta h + \frac{\partial \mathcal{N}_k^p}{\partial p_{i,j_k}^{n+1}} \Delta p = f_k^p - \mathcal{N}_k^p \left(\underline{h}_k^{n+1}, \underline{p}_k^{n+1} \right) \ , \tag{23}$$

for the increments $\Delta h_{i,j_k}$ and $\Delta p_{i,j_k}$ which are used to obtain the next approximation to the solution of the discretised equations on $\mathcal{G}_k$, via:

$$\widetilde{h_{0i,j_k}}^{n+1} = h_{0i,j_k}^{n+1} + \Delta h_{i,j_k} \ , \tag{24}$$

$$\widetilde{p_{0i,j_k}}^{n+1} = p_{0i,j_k}^{n+1} + \Delta p_{i,j_k} \ . \tag{25}$$

On the domain boundaries, Dirichlet conditions are resolved by assigning exact values at boundary nodes, while Neumann conditions are imposed by introducing additional ghost nodes outside the computational domain.

3.3.4 Coarse Grid Solution

On the coarsest grid level, $\mathcal{G}_0$, the discretised equations (19) and (20) are solved using Newton iteration. Defining the Jacobian matrices as:

$$\underline{\underline{A}} = \frac{\partial \mathcal{N}_0^p}{\partial \underline{p}_0^{n+1}} \ , \quad \underline{\underline{B}} = \frac{\partial \mathcal{N}_0^p}{\partial \underline{h}_0^{n+1}} \ , \quad \underline{\underline{C}} = \frac{\partial \mathcal{N}_0^h}{\partial \underline{p}_0^{n+1}} \ , \quad \underline{\underline{D}} = \frac{\partial \mathcal{N}_0^h}{\partial \underline{h}_0^{n+1}} \ , \tag{26}$$

the linearised solution to the coarse grid equations (19) and (20) are obtained by solving:

$$\underline{\underline{A}}\, \underline{\Delta w}_0^p + \underline{\underline{B}}\, \underline{\Delta w}_0^h = f_0^p - \mathcal{N}_0^p \left(\underline{w}_0^h, \underline{w}_0^p \right) \ , \tag{27}$$

$$\underline{\underline{C}}\, \underline{\Delta w}_0^p + \underline{\underline{D}}\, \underline{\Delta w}_0^h = f_0^h - \mathcal{N}_0^h \left(\underline{w}_0^h, \underline{w}_0^p \right) \ . \tag{28}$$

where $(\underline{w}_0^h, \underline{w}_0^p)$ and $\underline{\Delta w}_0^h, \underline{\Delta w}_0^p$ denote the first approximation to the coarse grid solution and its increments, respectively. The former are obtained as follows. First set $\underline{\Delta w}_0^h = \underline{0}$ to yield an initial approximation to $\underline{\Delta w}_0^p$, via:

$$\underline{\Delta w}_0^p = \underline{\underline{A}}^{-1} \left(f_0^p - \mathcal{N}_0^p \left(\underline{w}_0^h, \underline{w}_0^p \right) \right) \ . \tag{29}$$

Eliminating $\underline{\Delta w}_0^p$ from equations (27) and (28) gives the equation for $\underline{\Delta w}_0^h$, with:

$$(\underline{\underline{D}} - \underline{\underline{C}}\underline{\underline{A}}^{-1}\underline{\underline{B}})\underline{\Delta w}_0^h = f_0^h - \mathcal{L}_0^h\left(\underline{w}_0^h, \underline{w}_0^p\right) - \underline{\underline{C}}\underline{\Delta w}_0^p \ , \tag{30}$$

the solution of which is then used to obtain the next approximate solution, $(\underline{w}_0^h, \underline{w}_0^p)$, from:

$$\underline{w}_0^h \rightarrow \underline{w}_0^h + \underline{\Delta w}_0^h, \tag{31}$$
$$\underline{w}_0^p \rightarrow \underline{w}_0^p + \underline{\Delta w}_0^p - \underline{\underline{A}}^{-1}\underline{\underline{B}}\underline{\Delta w}_0^h \ . \tag{32}$$

This iterative process continues until the norm:

$$\frac{\sqrt{|f_0^p - \mathcal{N}_0^p\left(\underline{w}_0^h, \underline{w}_0^p\right)|^2 + |f_0^h - \mathcal{N}_0^h\left(\underline{w}_0^h, \underline{w}_0^p\right)|^2}}{n_c} \ , \tag{33}$$

where $n_c = 2^{c+1} + 1$ is the number of nodes in each direction on $\mathcal{G}_0$, is sufficiently small. An adequate convergence criterion is that the residual should be reduced below 0.1% of the value obtained using the initial estimate from the previous time step.

3.4 Adaptive Local Mesh Refinement

The incorporation of mesh adaptivity into a Multigrid framework has been reported in a variety of different contexts and includes the Multi-Level Adaptive Technique (MLAT) first proposed by Brandt [35], the Fast Adaptive Composite (FAC) of McCormick [39] and the Full Adaptive Multigrid (FAMe) of Rüde [40]. In each of these approaches adaptivity is implemented through a dynamic selection phase of local grid refinement which exploits the robustness of the underlying Multigrid solver. The first of these, MLAT, facilitates grid adapta-

tion procedures on different refinement levels by making full use of both local truncation error estimations and FAS and underpins the approach adopted.

3.4.1 Local Truncation Error Analysis

The motivation for implementing automatic mesh adaptivity is to enable the effects of small, isolated topographic features and specific groupings of the same to be captured accurately and efficiently so that fine grids are only deployed in areas where the flow is changing rapidly. An important issue with any mesh adaptivity scheme is the quantification of errors since these are used to identify those areas requring further refinement [41]. As noted in [38], the τ-indicator adopted in the present work is a natural choice for quantifying errors since information is readily available from the different grid levels. The difference in truncation error on successive grids $\mathcal{G}_k$ and $\mathcal{G}_{k-1}$ is approximated via a relative truncation error quantity, τ_k^{k-1}, with large values of τ_k^{k-1} indicating regions of significant error between successive grid levels and where correspondingly further grid refinement is necessary.

Since the local truncation error term τ_k measures the difference between the discrete and the continuous problem:

$$\tau_k = \mathbf{N}_k(\mathbf{u}_k) - \mathbf{f}_k \ , \tag{34}$$

which can be re-arranged so that τ_k is regarded as the correction in equation (21) of the Multigrid process, via:

$$\tau_k^{k-1} = \mathbf{N}_{k-1}(R_k^{k-1}\tilde{\mathbf{u}}_k) - R_k^{k-1}(\mathbf{N}_k\tilde{\mathbf{u}}_k) \ , \tag{35}$$

where $\tilde{\mathbf{u}}_k$ is the solution on $\mathcal{G}_k$ at the coarse grid correction stage. The criterion for grid refinement can then be defined against a given user specified tolerance

ε, where the grids are refined locally whenever $\tau_k^{k-1} \geq \varepsilon$. Note that τ_k^{k-1} is also used here as a natural stopping criterion to prevent unnecessary Multigrid iterations when residuals are already dominated by the local truncation error.

3.4.2 Conservative Interpolation

A general approach to the discretisation at local refinement interfaces is to conserve numerical flux at both the coarse and fine locally refined regions (see for e.g. [25]). As explained in [37], the numerical flux across a control volume is defined in terms of a surface integral across its boundaries in the form:

$$F = \int\int_S \underline{u} \cdot \underline{n} \, dS \ , \tag{36}$$

where,

$$\underline{u} = \underline{u}_h = \left(\frac{h^3}{3} \left(\frac{\partial p}{\partial x} - 2 \right), \frac{h^3}{3} \left(\frac{\partial p}{\partial y} \right) \right), \tag{37}$$

for equation (13) and,

$$\underline{u} = \underline{u}_p = -\frac{6}{\beta^3} \nabla (h + s) \ , \tag{38}$$

for equation (14).

By introducting additional, *ghost* nodes around the interfaces of these locally refined boundaries, the adaptive Multigrid process is straightforward, where standard multigrid techniques can be used on all points in the refined region as well as those at the interfaces [38]. The relationship between the coarse $\mathcal{G}_{k-1}$ and fine $\mathcal{G}_k$ grid levels is illustrated in Figure 4. If the composite grid, $\mathcal{G}_k^{k-1} = \mathcal{G}_{k-1} \cap \mathcal{G}_k$, denotes a set of overlapping nodes, coarse grid nodes that do not coincide with the overlapping regions, i.e. in $\mathcal{G}_{k-1} \backslash \mathcal{G}_k^{k-1}$, correspond to

fine grid nodes on subsequent coarser grid levels.

Figure 5 shows a composite mesh with nodes located at the boundary between coarse and fine grids of mesh sizes Δ_{k-1} and Δ_k, respectively. The values of the ghost nodes are predicted by imposing the flux across control volume V_1, illustrated in figure 5(a), as equal to that in V_2, depicted in figure 5(b). Numerical flux conservation across the interface of the darker shaded regions V_1 and V_2 requires that:

$$\frac{F(V_1)}{3\Delta_k^2/2} = \frac{F(V_2)}{\Delta_k^2/2} \ . \tag{39}$$

The flux G_e, shown in figure 5(b), is the flux across the articifial eastern boundary introduced by the presence of the ghost nodes. Its value is given by:

$$G_e = \frac{2F_e + F_w}{3} \ , \tag{40}$$

where F_w denotes the flux across the western cell boundary and

$$F_e = \frac{1}{2}(F_u + F_d) \ , \tag{41}$$

is the average flux across the eastern cell boundary, with F_u and F_d the fluxes across the coarse volumes on V_2 for the case shown in figure 5(a).

Using the lubrication equations, the values at the ghost nodes derived from equations (40) and (41) across the eastern interface boundary for equations (13) and (14) are given by:

$$p^g_{i,j} = \frac{\Delta(G^h_e + 2(h^3/3)|_{i-1/2,j})}{(h^3/3)|_{i-1/2,j}} + p_{i-1,j} \ , \tag{42}$$

$$h^g_{i,j} = \frac{\Delta G^p_e \beta^3}{6} + (h_{i-1,j} - s_{i-1,j}) - s_{i,j} \ . \tag{43}$$

Similar expressions may be derived for ghost nodes along the western, northern and southern interface boundaries [42].

3.5 Implementing Adaptivity within the Multigrid Algorithm

Due to the use of a MLAT framework and employing vertex-centred discretisation on uniform quadrilateral grids, implementing automatic mesh adaptivity selectively is reasonably straight forward. In overlapping local grid regions, the discrete form of the governing lubrication equations (19) and (20) are modified to account for the effects of non-uniform grid resolution, in so much as the modified form of the coarse grid correction scheme from equation (21), is rewritten as:

$$\mathbf{N}_{k-1}\mathbf{w}_{k-1}^{m} = \mathbf{f}_{k-1} \ , \tag{44}$$

where

$$\mathbf{f}_{k-1} = \begin{cases} \mathbf{f}_{k-1} & \text{on non-overlapping grid regions, } \mathcal{G}_{k-1}\backslash\mathcal{G}_{k}^{k-1} \ , \\ \mathbf{d}_{k-1}^{m} + \mathbf{N}_{k-1}\tilde{\mathbf{u}}_{0}{}_{k-1}^{m} & \text{on overlapping grid regions } \mathcal{G}_{k}^{k-1} \ . \end{cases} \tag{45}$$

Likewise, coarse grid solutions on $\mathcal{G}_{k-1}$ are defined by:

$$\tilde{\mathbf{u}}_{0}{}_{k-1}^{m} = \begin{cases} \tilde{\mathbf{u}}_{0}{}_{k-1}^{m} & \text{on non-overlapping grid regions, } \mathcal{G}_{k-1}\backslash\mathcal{G}_{k}^{k-1} \ , \\ R_{k}^{k-1}\tilde{\mathbf{u}}_{0}{}_{k}^{m} & \text{on overlapping grid regions } \mathcal{G}_{k}^{k-1} \ . \end{cases} \tag{46}$$

In order to conserve flux across fine and coarse interface boundaries, information from ghost nodes is incorporated using equations (42) and (43). Using ghost nodes around the interface boundaries enables the standard Multigrid restriction and prolongation operators to be used. In most cases, the ghost nodes can simply be treated as Dirichlet boundary points and their values only updated from the coarse grid correction at the end of the Multigrid iteration. However, when the ghost nodes intersect the domain boundaries they use the global boundary conditions instead. A pseudo-code description of the Adaptive Multigrid Cycle is:

Adaptive FAS Cycle $\mathbf{u}_{1_k}^{m+1} = \text{ADPFASCYC}(k, \mathbf{u}_{0_k}^{m}, \mathbf{f}_k, \tau_k^{k-1}, \nu_1, \nu_2, \kappa)$

- Pre-relaxation:
  - Perform ν_1 relaxation sweeps:

    $\tilde{\mathbf{u}}_{0_k}^{m} = \text{RELAX}(\mathbf{u}_{0_k}^{m}, \mathbf{f}_k)$
- Coarse grid correction:
  - Compute residual on $\mathcal{G}_k$

    $\mathbf{d}_k^m = \mathbf{f}_k - \mathbf{N}_k \tilde{\mathbf{u}}_{0_k}^{m}$
  - Restrict residual to next coarser grid level from $\mathcal{G}_k$

    $\mathbf{d}_{k-1}^m = R_k^{k-1} \mathbf{d}_k^m$
  - Compute coarse grid solution on $\mathcal{G}_{k-1}$ according to equation (46)
  - Compute right hand side on $\mathcal{G}_{k-1}$ according to equation (45)
  - Calculate local truncation error τ_k^{k-1} according to equation (35)
  - If $k = 1$, solve solution on coarsest grid,

    $\mathbf{N}_{k-1} \mathbf{w}_{k-1}^m = \mathbf{f}_{k-1}$

    If $k > 1$, perform κ iterations using $\tilde{\mathbf{u}}_{0_{k-1}}^{m}$ as initial approximation,

$\mathbf{w}_{k-1}^m = \text{ADPFASCYC}(k-1, \tilde{\mathbf{u}}_{0\,k-1}^m, \mathbf{f}_{k-1}, \tilde{\tau}_{k-1}^{k-2}, \nu_1, \nu_2, \kappa)$

- Compute corrections on $\mathcal{G}_k^{k-1}$ with,

  $\mathbf{v}_{k-1}^m = \mathbf{w}_{k-1}^m - \tilde{\mathbf{u}}_{0\,k-1}^m$

  or set the solution on $\mathcal{G}_{k-1}$ with,

  $\mathbf{u}_{0\,k-1}^m = \mathbf{w}_{k-1}^m$

- Interpolate corrections onto $\mathcal{G}_k$

  $\mathbf{v}_k^m = I_{k-1}^k \mathbf{v}_{k-1}^m$

- Update approximated solution on $\mathcal{G}_k$ with,

  $\mathbf{u}_{0\,k}^m = \tilde{\mathbf{u}}_{0\,k}^m + \mathbf{v}_k^m$

- Post-relaxation:

  - Perform ν_2 relaxation sweeps: $\mathbf{u}_{1\,k}^{m+1} = \text{RELAX}(\mathbf{u}_{0\,k}^m, \mathbf{f}_k)$

4 Results

Unless stated otherwise stated the accuracy and efficiency of the adaptive Multigrid solver is demonstrated by solving the flow of thin water films of asymptotic film thickness $H_0 = 100\mu m$, viscosity $0.001\text{Pa}\,\text{s}$, density $\rho = 1000\text{kg}\,\text{m}^{-3}$ and surface tension $\sigma = 0.07\text{N}\,\text{m}^{-1}$ down a substrate inclined at 30° to the horizontal and with a constant inlet flow rate $Q_0 = 1.635 \times 10^{-6}\text{m}^2\text{s}^{-1}$ [5]. These parameters yield a Capillary length $L_c = 0.78\text{mm}$ and $N = 0.122$, the latter value indicating that gravity has little influence on the free surface shape. All results are obtained using an FMG V(4,2) cycle with a coarse grid constant $c = 2$ (9x9 nodes in each direction) with finest grid levels $k \leq 6$.

The first problem considered is that of steady flow over a square trench with $s_0 = -0.1(10\mu m)$, $l_t = w_t = 0.1(3.9mm)$ and $\gamma = 0.05$, centred at

$(x_t, y_t) = (0.35, 0.5)$. Figure 6 explores the evolution of the free surface, $(h+s)$, at different time levels. To aid visualisation of the computational grids, the underlying uniform global grid level is set at $k = 2$ (33x33 nodes) and the grid is permitted to adaptively refine itself over the next two finer grid levels, corresponding to $3 \leq k \leq 4$, with spatial increments, $\Delta = 1/64$ and $\Delta = 1/128$, respectively. The mesh adaptivity tolerance is set to $\varepsilon = 0.1\tau_k^{k-1}$ and the topography sides are indicated by the white square outline residing within the region of greatest grid adaptation.

Starting with an initially flat free surface profile, $(h + s) = 1$, the problem is solved at successive time steps until a steady state is reached. For $t = 0.1$, Figure 6(a) shows how the Capillary ridge is initially formed upstream of the trench while fluid surges out of the trench in the downstream direction. At the later times $t = 0.2$ and $t = 0.3$, shown in Figures 6(c)-(f), although mesh adaptivity remains concentrated around the Capillary ridge and downstream surge it also follows the developing bow wave that is shed from the sides of the trench. The features are shown clearly at $t = 1.0$ by which time the flow has reached its steady state. Figure 7 illustrates how the region of grid adaption is affected by the mesh adaptivity tolerance: plan views of the steady state grid are shown for $\varepsilon = 0.05\tau_k^{k-1}$ and $\varepsilon = 0.02\tau_k^{k-1}$ with topographic sides again indicated in white outline. As expected, smaller values of ϵ increase the sensitivity of the adaptivity process, thereby expanding the areas of local mesh refinement in regions of largest flow gradients.

The benefits of automatic local adaptivity become even clearer when solving flow over smaller topographies where a regular uniform mesh requires overall fine grid resolution to achieve grid independent solutions. Figure 8 considers flow over a square trench topography of depth $10\,\mu m$ where its sides have

been reduced from $3.9\,mm$ to $0.78\,mm$, showing the streamwise free surface profiles at $y = 0.5$ and spanwise free surface profiles at $x = 0.5$ obtained non-adaptively with uniform global grid levels $4 \leq k \leq 6$. Figure 8(a) shows that the uniform 129x129 grid ($k = 4$) is clearly too coarse to capture the flow over the topography while a 513x513 one is needed to achieve grid-independent solutions in the downstream surge region. This is shown more clearly by the spanwise profiles at $x = 0.5$ given in Figure 8(b) where large discrepancies are seen even when a uniform 257x257 grid is employed.

The above, uniform mesh profiles, are now compared with those obtained adaptively. Once again, a coarse 33x33 underlying global grid is used while local grid refinement is permitted over a maximum of either three or four grid levels, i.e. local grid densities up to $k = 5$ or $k = 6$ respectively. The mesh adaptivity tolerance between adjacent grid levels is set to $\varepsilon = 0.1\tau_k^{k-1}$. The streamwise profiles along $y = 0.5$ shown in Figure 9(a) demonstrate that, even with a coarse underlying global grid, the adaptive solutions are in excellent agreement with the fine-mesh non-adaptive results. The corresponding comparison is made in Figure 9(b) for spanwise profiles at $x = 0.5$. Again, in both cases the non-adaptive profiles agree accurately with the ones obtained adaptively, for which the mesh is allowed to refine locally to the same fine grid density. Indeed in all cases the maximum deviation between free-surface profiles found adaptively and non-adaptively is less than 0.05%.

Increasing computational efficiency, while retaining solution accuracy, is a prime motivation for adopting an effective adaptive meshing strategy. Figure 10(a) compares the number of fine-grid nodes needed non-adaptively with the number of nodes required with adaptivity, as a function of the mesh adaptivity tolerance, for a specified finest grid level k, in solving the problem of

flow over a square trench. Prescribing a smaller tolerance inevitably leads to an increased number of nodes as the locally refined regions expand. For the case with $\varepsilon = 0.1\tau_k^{k-1}$, whose accuracy has already been demonstrated in Figure 9, the adaptive Multigrid solutions require less than 4% of the grid nodes needed to obtain an equally accurate solution on a uniform mesh with $k = 6$. Figure 10(b) shows how the smaller number of grid nodes translates into increased computational efficiency. It demonstrates, first of all, that the adaptive solver is effectively achieving the desired $O(N)$ efficiency (N is the number of unknowns) and, secondly, that the approach yields significant computational savings. For a finest grid level of $k = 6$, for example, mesh adaptivity with $\varepsilon = 0.1\tau_k^{k-1}$ require less than 10% of the CPU time needed to obtain an equivalent non-adaptive fine-mesh solution. Note also that decreasing the mesh adaptivity tolerance parameter has less effect on CPU time than it does on the number of grid nodes, since the majority of the additional nodes introduced by reducing ε are confined to the coarser grid levels where relaxation is less computationally expensive.

Another important benefit of automatic grid adaption is that it offers the flexibility and efficiency needed to solve flow past topography of various shape. Figure 11 shows the free-surface profiles obtained for steady flows over diamond and circular trenches, each of depth $10\,\mu m$ and with edges that do not coincide with the (x, y) coordinate directions. The diamond trench is formed by rotating the square trench prescribed by equation (9), through 45° where once again s_0 is the depth and (x_t, y_t) is the centre of the diamond. The circular trench topography is similarly given by:

$$s(x, y) \;=\; \frac{s_0}{b_0}\; tan^{-1}\left(\frac{r - r_t}{\gamma r_t}\right) \;, \tag{47}$$

where $r = \sqrt{(x - x_t)^2 + (y - y_t)^2}$, r_t is its radius and b_0 and γ are as defined previously. As in Figure 6, for reasons of clarity, the sides of the trench have been increased so that $l_t = w_t = 2r_t = 0.1$. Grid adaptivity takes place over a maximum of two grid levels from the underlying uniform 33x33 global coarse mesh, in the vicinity of the topographies themselves, with only a single level of local refinement taking place in the bow wave region. This can be seen clearly in the plan views of the adaptive grid structures shown in Figures 11(b) and 11(d).

The steady state solution shown in Figure 12 further illustrates the flexibility of automatic adaptivity by solving for the flow over five discrete topographies where a central, diamond-shaped trench with $s_0 = -0.1$ and $w_t = l_t = 0.05$ is surrounded by two equally-sized circular peaks upstream, with $s_0 = 0.15$ and $2r_t = 0.05$ and two circular trenches downstream, with $s_0 = -0.15$ and $2r_t = 0.05$. Here the underlying uniform global coarse grid level is set to $k = 2$ (33x33) while local grid refinements are performed using adaptivity tolerance, $\varepsilon = 0.05\tau_k^{k-1}$. Figure 12(b), depicts the resultant steady-state free-surface profile, while Figure 12(c) shows the automatic local grid adaption that is required to produce accurate solutions. Once again, the greatest refinement is concentrated near the topographies themselves and in a ring around the central diamond-shaped trench, which is seen much more clearly now that the size of the Capillary ridge and bow wave disturbances have been significantly reduced by the presence of the surrounding circular peaks and trenches.

If the industrial goal, for example, is to planarise the free surface it would be necessary to use a more sophisticated combination of isolated topographies. Figure 13 considers the simpler problem of mitigating free surface disturbances

in the streamwise profile at $y = 0.5$, the challenge being to reduce the size of the free surface depression over the diamond trench with minimal disturbances elsewhere. The adaptive solver enables several different candidate topography configurations to be tested efficiently and accurately. Figure 13 shows one such example where the streamwise profile is much reduced by positioning the circular topographies closer to the central, diamond-shaped one. The geometrical arrangement shown in Figure 13(a) leads to significant reductions in the streamwise free surface profile, Figure 13(b). Figure 13(c) shows the corresponding adaptive and non-adaptive free surface profiles for the geometrical arrangements shown in Figures 12(a) (case 1) and 13(a) (case 2); once again the agreement between them is excellent, with maximum differences in film thickness less than 0.2%. Apart from minor differences in the Capillary ridge and surge regions, the free surface profile for case 1 is similar to that found for flow past an isolated diamond trench. The second configuration is much more successful in reducing the free surface disturbances, where an 80% reduction in the large depression can be achieved without persistent disturbances to the downstream free surface profile.

The final set of solutions highlight the performance of the adaptive Multigrid solver for time-dependent flow over topography, see [15]; here, following [20], time-dependent flow over a square trench topography is considered ($s_0 = -0.5$, $w_t = l_t = 0.1$). Adaptive Multigrid solutions are given which use an underlying uniform 65x65 coarse grid ($k = 3$) with a further three levels of local refinement permitted according to the criterion $\varepsilon = 0.05\tau_k^{k-1}$. Following [15], starting from a steady state condition with a uniform flow rate, the film thickness at the inlet boundary $x = 0$ is varied sinusoidally according to:

$$h = 1 + 0.2\sin(2\pi f t) \ , \tag{48}$$

where f is the frequency of oscillation.

Figure 14 shows the free surface profiles for two different frequencies, $f = 4\,Hz$ and $f = 10\,Hz$, at $t = 0.1$ and $t = 0.35$, the oscillation beginning at $t = 0$. Further numerical solutions at later times confirm that the flow displays a periodic behaviour according to the frequency of excitation. As noted by Sellier [20], the higher frequency fluctuations generate high curvature regions that are quickly smoothed out by surface tension with the result that free surface disturbances are much larger for the lower frequency. Note, however that for the latter case the sinusoidal free surface fluctuation is distorted by the presence of the topography.

Figure 15 shows corresponding free surface profiles along $y = 0.5$ obtained adaptively and non-adaptively, compared to the steady state profile with a uniform flow rate. Once again agreement between the two is excellent at all times. Both frequencies show the formation of a surge hump downstream of the topography, which may be thought of as a solitary wave. The speed of these waves is found to be approximately equal to $2U_0$, a value that is consistent with earlier findings [15].

5 Conclusion

Thin film and spreading flows over topographically heterogeneous substrates are of enormous significance in a variety of biological, scientific and industrial processes. However despite their practical significance their numerical modelling is only at an early stage of development, previous studies having been limited to flows over relatively simple topographic shapes. In this paper a

new Multigrid strategy embodying a lubrication flow solver with automatic mesh adaption for investigating the important problem of thin film flow over arbitary topography (peaks, trenches and their combination) is described. It is shown to be well-suited to simulating thin film flow over distributions of topographies of arbitrary cross-section, offering significant memory and computational savings compared to existing, non-adaptive methods. The efficiency and accuracy of the solver is demonstrated and compared with corresponding solutions obtained on a uniform fine mesh for the case of thin film flow past a small square trench topography. Also, results for such flow over different trench shapes have highlighted the adaptive solvers' ability to create fine meshes only in regions exhibiting large gradients in the free surface, namely over the topography itself, in the Capillary ridge and in the downstream surge and characteristic bow wave.

The solver is an important development towards the production of practically useful simulation tools that can solve real problems, for example identifying the opotimum secondary topography distribution needed as part of a manufacturing process to planarise free surface flows over desirable topography [5]. The alternative of using localised heating as a means of inducing Marangoni stresses to promote levelling [43] has been suggested for this purpose. However, the drawbacks in terms of cost, and feasibility in the case of small topography, are considerable. The present work also has natural extensions to a range of other important thin film flow problems where the effects of, for example, solvent evaporation [23], are influential, or even to the wide range of thin film spreading flows where contact line migration and wetting phenomena are key [1].

References

[1] Liquid Film Coating. In: Kistler SF, Schweizer PM, editors. Chapman & Hall; 1997.

[2] Jensen OE, Chini GP, King JR. Thin-film flows near isolated humps and interior corners. J. Eng. Math. 2004; 50: 289-309.

[3] Braun RJ, Fitt AD. Modelling drainage of the precorneal tear film after a blink. Math. Med. Biol. 2003; 20: 1-28.

[4] Abu-Ramadan E, Khayat RE. Shear-thinning flow in weakly modulated channels. Int. J. Numer. Meth. Fluids 2005; 48: 467-99.

[5] Decre MJ, Baret JC. Gravity driven flows of viscous liquids over two-dimensional topographies. J. Fluid Mech. 2003; 487: 147-66.

[6] Peurrung LM, Graves BG. Spin coating over topography. IEEE Trans. Semi. Man. 1993; 6: 72-6.

[7] Kalliadasis S, Homsy GM. Steady free-surface thin film flow over two-dimensional topography. Phys. Fluids 2000; 12: 1889-98.

[8] Kalliadasis S, Homsy GM. Stability of free surface thin-film flows over topography. J. Fluid Mech. 2001; 448: 387-410.

[9] Wierschem A, Scholle M, Aksel N. Vortices in film flow over strongly undulated bottom profiles at low Reynolds numbers. Phys. Fluids 2003; 15(2): 426-35.

[10] Vlachogiannis M, Bontozoglou V. Experiments on laminar film flow along a periodic wall J. Fluid Mech. 2002; 457: 133-56.

[11] Wierschem A, Scholle M, Aksel N. Comparison of different theoretical approaches to experiments on film flow down an inclined wavy channel. Experiments in Fluids 2002; 33: 429-42.

[12] Pozrikidis C. Effect of surfactants on film flow down a periodic wall. J. Fluid Mech. 2003; 496: 105-27.

[13] Pozrikidis C, Thoroddsen ST. The deformation of a liquid film flowing down an inclined plane wall over a small particle arrested on the wall. Phys. Fluids 1991; 11(a): 2546-59.

[14] Hayes M, O'Brien SBG, Lammers JH. Green's function of steady flow over a two-dimensional topography. Phys. Fluids 2000: 12: 2845-58.

[15] Bielarz C, Kalliadasis S. Time-dependent free surface thin film flows over topography. Phys. Fluids 2003; 15(9): 2512-24.

[16] Christov CI, Pontes J, Walgraef D, Velarde MG. Implicit Time Splitting for Fourth-Order Parabolic Equations. Comp. Meth. Appl. Mech. Engrg. 1997; 148: 209-24.

[17] Schwartz LW, Eley RR. Simulation of droplet motion on low energy and heterogeneous surfaces. J. Coll. Int. Sci. 1998; 202: 173-88.

[18] Daniels N, Ehret P, Gaskell PH, Thompson HM, Decre M. Multigrid methods for thin film spreading flows. In N. Satofuka, editor. Proc. 1st Conf. on CFD: Springer; 2001. p.279-84.

[19] Gaskell PH, Jimack PK, Sellier M, Thompson HM. Efficient and accurate time adaptive multigrid simulations of droplet spreading. Int J. Numer. Meth. Fluids 2004; 45: 1161-86.

[20] Sellier M. PhD thesis. University of Leeds; 2003.

[21] Mazouchi A, Homsy GM. Free surface Stokes flow over topography. Phys. Fluids 2001; 13: 2751-61.

[22] Gaskell PH, Jimack PK, Sellier M, Thompson HM, Wilson MCT. Gravity-driven flow of continuous thin liquid films on non-porous substrates with

topography. J. Fluid Mech. 2004; 509: 253-80.

[23] Gaskell PH, Jimack PK, Sellier M, Thompson HM. Flow of evaporating, gravity-driven thin liquid films over topography. Phys. Fluids 2006; 18: 031601.

[24] Bai D, Brandt A. Local Mesh Refinement Multilevel Techniques. SIAM J. Sci. Stat. Comput. 1987; 8(2): 109-34.

[25] Douglas CC, Hy J, Ray J, Thorne DT, Tuminaro RS. Cache aware multigrid for variable coefficient elliptic problems on adaptive mesh refinement hierarchies. Numerical Linear Algrebra and Applications 2004; 11: 173-87.

[26] Thompson MC, Ferziger JH. An adaptive multigrid technique for the incompressible Navier-Stokes equations. J. Comp. Phys. 1989; 82: 94-121.

[27] Berger MJ, Colella P. Local adaptive mesh refinement for shock hydrodynamics. J. Comp. Phys. 1989; 82: 64-84.

[28] Braaten ME, Connell SD. Three-dimensional unstructured adaptive multigrid scheme for the Navier-Stokes equations. AIAA Journal 1996; 34(2): 281-90.

[29] Lee YC. PhD thesis. University of Leeds; 2004.

[30] Goodyer CE, Fairlie R, Berzins M, Scales LE. Adaptive mesh methods for elastohydrodynamic lubrication. ECCOMAS CFD Conference; 2001.

[31] Trangenstein JA, Kim C. Operator Splitting and Adaptive Mesh Refinement for the Luo-Rudy I Model. J. Comput. Phy. 2004; 196: 645-79.

[32] Schmidt GH, Jacobs FJ. Adaptive local grid refinement in multi-grid numerical reservoir simulation. J. Comp. Phys. 1988; 77: 140-65.

[33] Aksel N. Influence of the capillarity on a creeping flow down an inclined plane with an edge. Arch. Appl. Mech. 2000; 70: 81-90.

[34] Kondic L, Diez J. Pattern formation in the flow of thin film down an inclined plane: constant fluz configuration. Phys. Fluids 2001; 13(11): 3168-84.

[35] Brandt A. Multi-Level Adaptive Solutions to Boundary-Value Problems. Math. Comp. 1977; 31: 333-90.

[36] Wesseling P. An Introduction to Multigrid Methods. John Wiley & Sons; 1992.

[37] Trottenberg U, Oosterlee CW, Schüller A. Multigrid. London: Academic Press; 2001.

[38] Brandt A. Multigrid Techniques: 1984 Guide with Applications to Fluid Dynamics. GMD-Studie Nr. 85, Sankt Augustin, West Germany; 1984.

[39] McCormick SF. Multilevel Adaptive Methods for Partial Differential Equations. In: Frontiers in Applied Mathematics 6. Philadelphia: SIAM; 1989.

[40] Rüde U. Fully adaptive multigrid methods. SIAM J. of Numer. Analy. 1993; 30(1): 230-48.

[41] Huerta A, Rodrguez-Ferran A, Dez P, Sarrate J. Adaptive finite element strategies based on error assessment. Int. J. Numer. Meth. in Engng. 1999; 46: 1803-18.

[42] Martin D, Cartwright K. Solving Poisson's equation using adaptive mesh refinement. Technical Report M96/66, Electronic Research Laboratory. Berkeley: University of California; 1996.

[43] Gramlich CM, Kalliadasis S, Homsy GM, Messer C. Optimal levelling of flow over one-dimensional topography by Marangoni stresses. Phys. Fluids. 2002; 14: 1841-50.

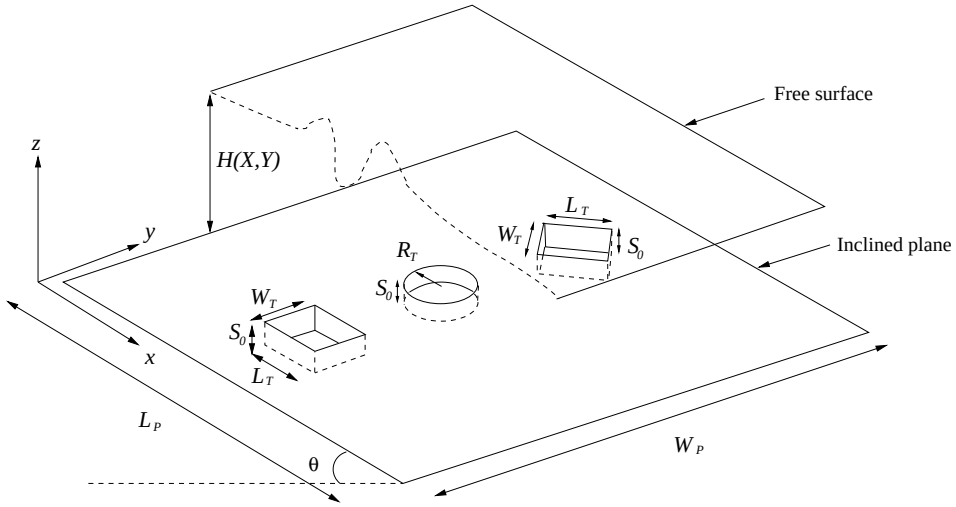

Fig. 1. A schematic diagram of gravity-driven thin film flow over three typical and well defined topographies: square, circular and diamond shaped trenches.

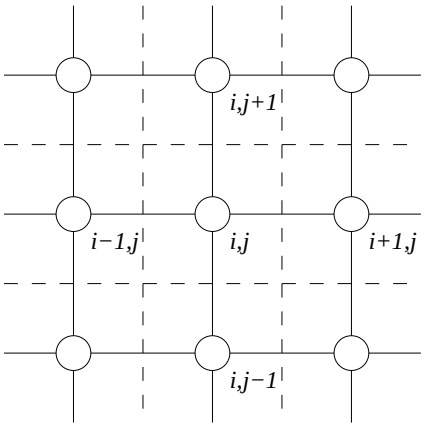

Fig. 2. A cell-vertex control volume, centred at the point (i, j), indicated by dashed lines, together with its surrounding neighbours.

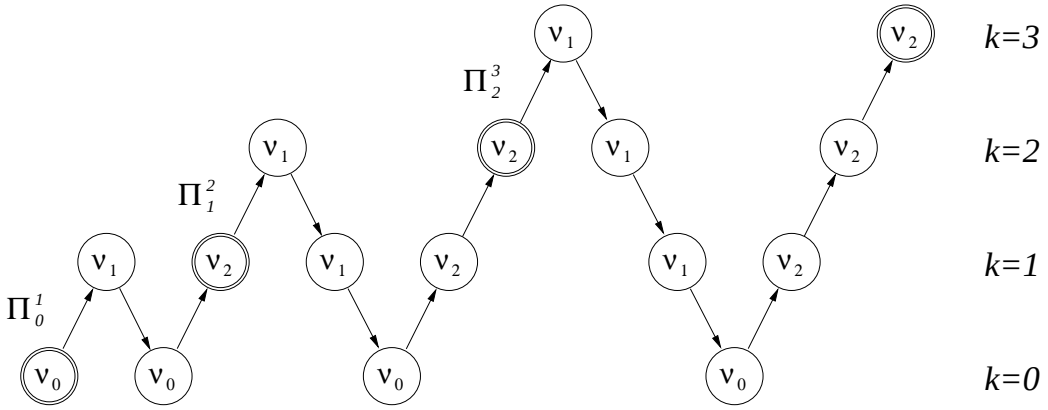

Fig. 3. Schematic representation of the full multigrid (FMG) algorithm over four grid levels.

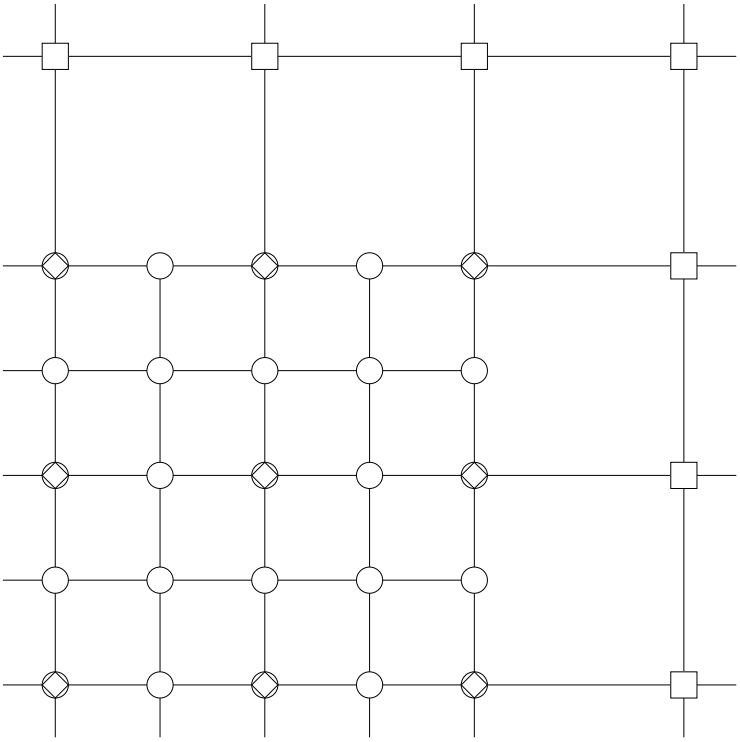

Fig. 4. A locally refined region on a two level composite mesh showing nodes on fine grid, $\mathcal{G}_k$, coarse grid, $\mathcal{G}_{k-1}$, and composite grid, $\mathcal{G}_k^{k-1}$, denoted by circles ($\circ$), squares ($\square$), and diamonds ($\diamond$), respectively.

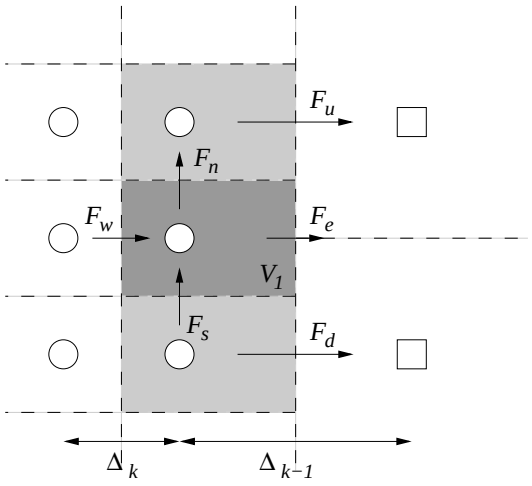

(a)

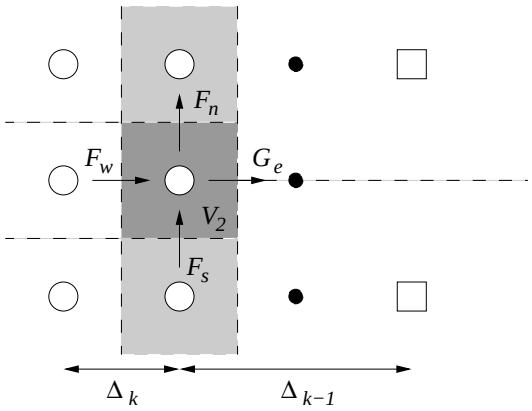

(b)

Fig. 5. Control volume: (a) V_1 original, and, (b) V_2 modified; along an eastern boundary interface, indicated by shaded regions between fine (○) and coarse (□) grid nodes, showing key fluxes across control volume boundaries and newly introduced ghost nodes, (•).

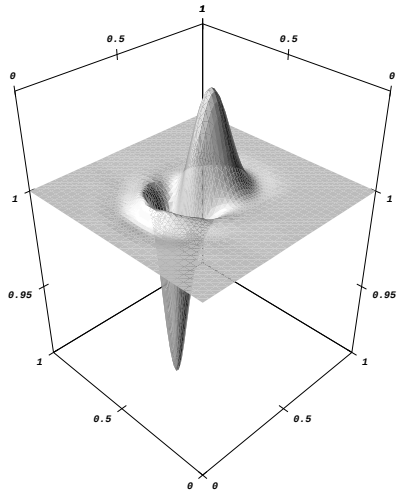

(a) t=0.1

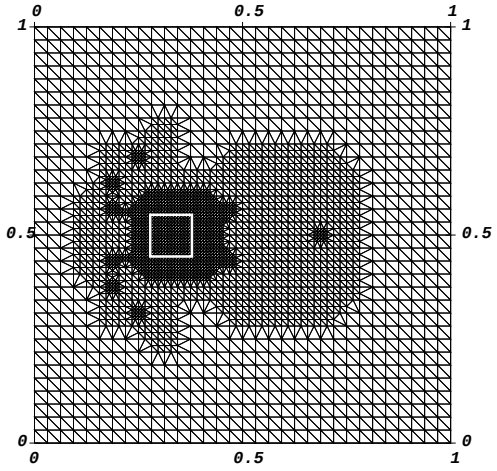

(b) t=0.1

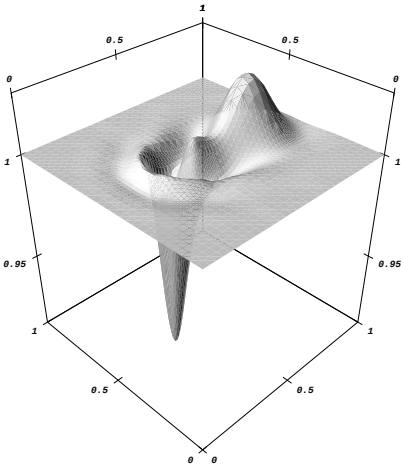

(c) t=0.2

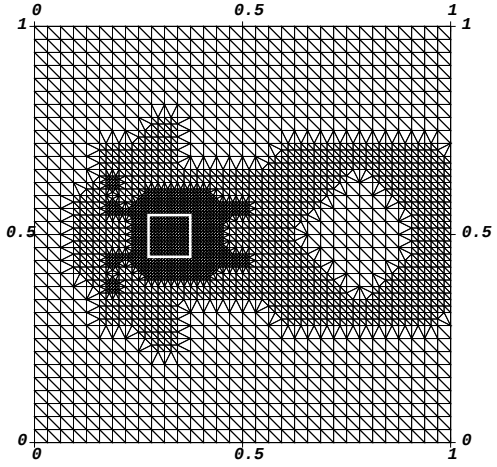

(d) t=0.2

Fig. 6. Time-dependent evolution of free surface, $h + s$ (left), and mesh (right), obtained using the global coarse grid, $k = 2$, with two levels of grid refinement and $\varepsilon = 0.1\tau_k^{k-1}$, for thin film flow over a square trench ($w_t = 0.1, s_0 = -0.1$). Four time intervals are shown, where $t = 1.0$ is steady-state.

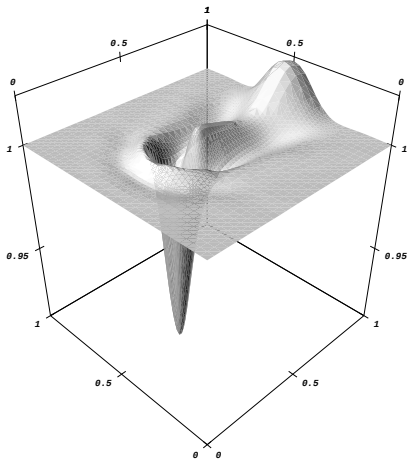

(e) t=0.3

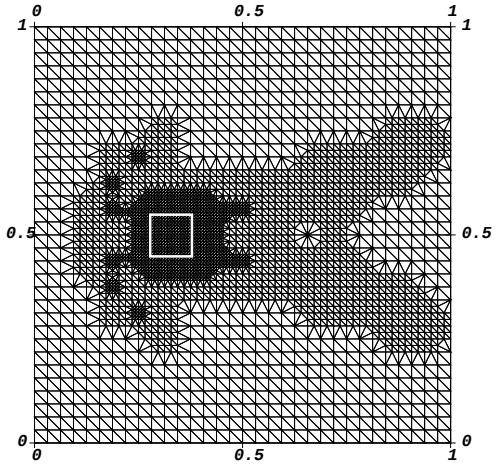

(f) t=0.3

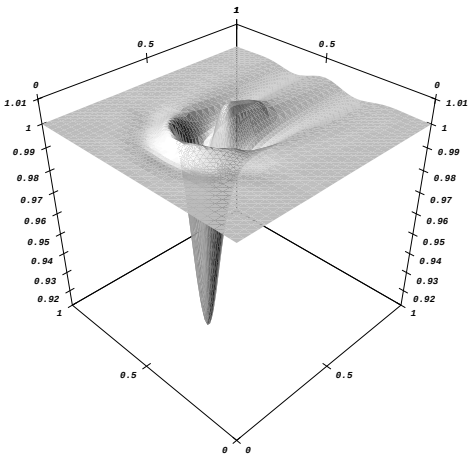

(g) t=1.0

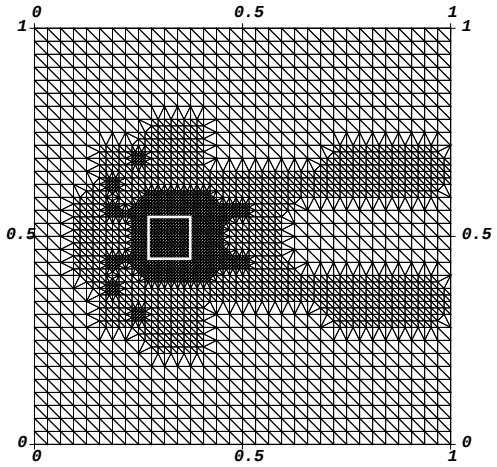

(h) t=1.0

Fig. 6. (continued.)

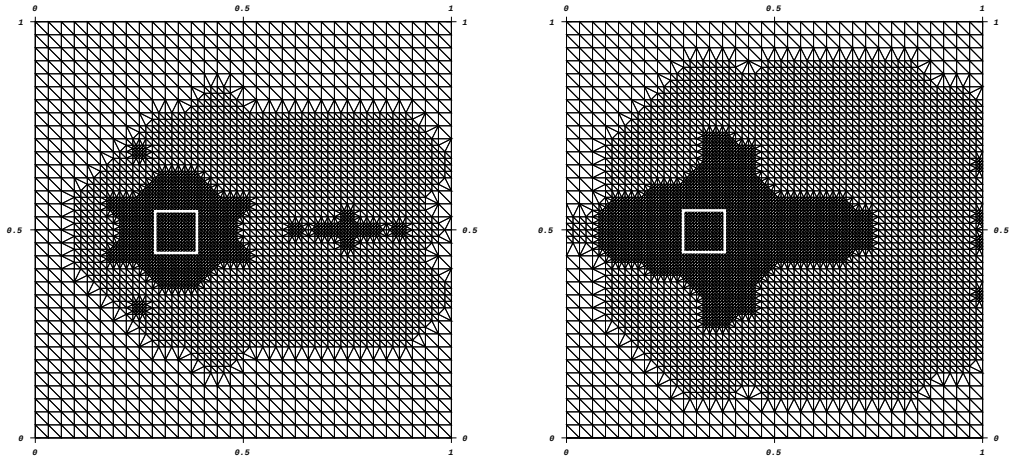

(a) (b)

Fig. 7. Steady-state mesh refinement distribution for the case of flow over a square trench topography ($w_t = 0.1, s_0 = -0.1$), built from a uniform global coarse grid $k = 2$, with two grid refinement levels, for different prescribed tolerence: (a) $\varepsilon = 0.05\tau_k^{k-1}$; (b) $\varepsilon = 0.02\tau_k^{k-1}$.

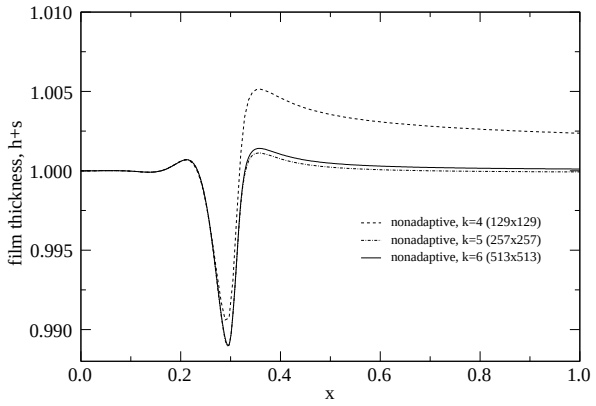

(a)

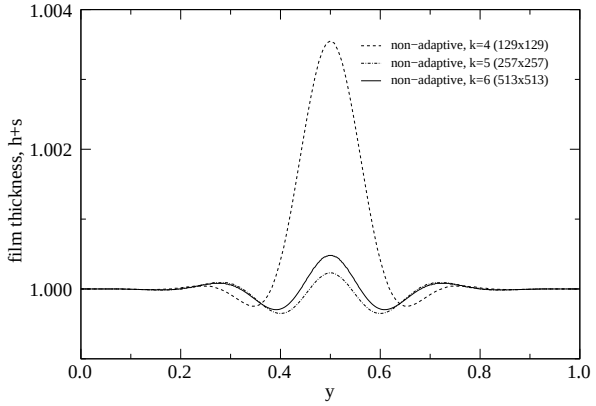

(b)

Fig. 8. (a) Streamwise, $y = 0.5$, and (b) spanwise, $x = 0.5$, free surfaces profiles for flow over a square trench ($w_t = 0.02, s_0 = -0.1$), obtained non-adaptively on the uniform fine meshes indicated.

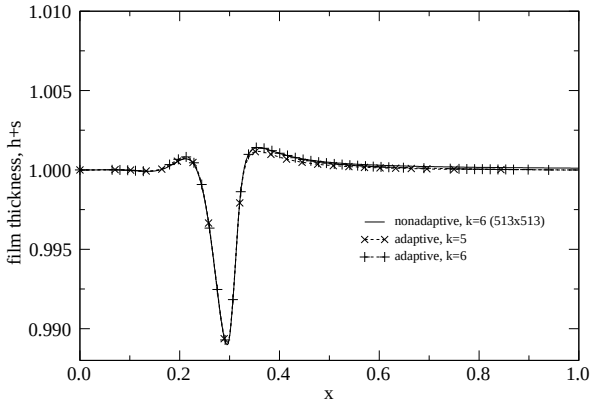

(a)

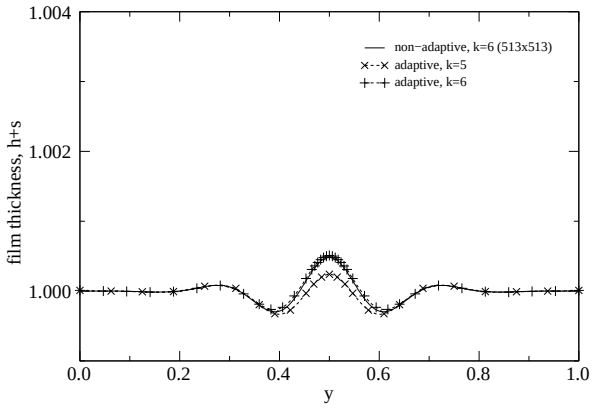

(b)

Fig. 9. Differences in (a) streamwise, $y = 0.5$, and (b) spanwise, $x = 0.5$, free surfaces profiles for flow over a square trench ($w_t = 0.02, s_0 = -0.1$), obtained both non-adaptively and adaptively.

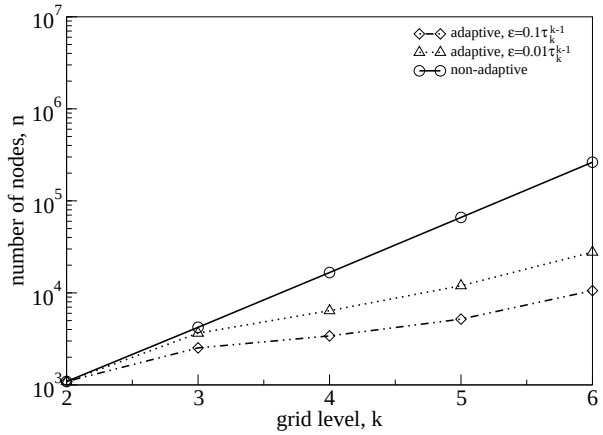

(a)

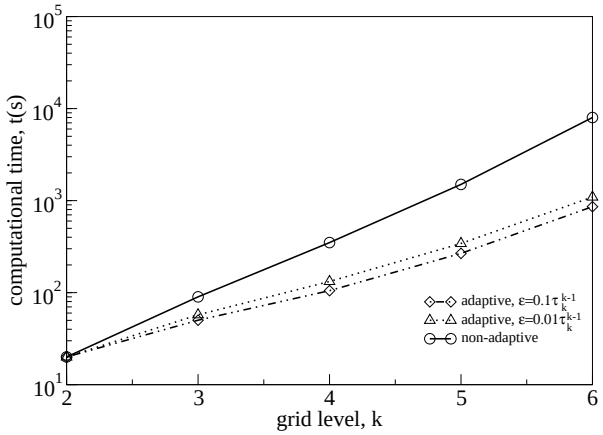

(b)

Fig. 10. Relative efficiency of the solver in terms of (a) number of nodes, and (b) CPU time, for the case of flow over a square trench ($w_t = 0.02, s_0 = -0.1$). Comparison is made between the efficiency of solutions obtained non-adaptively and adaptively, the latter with different tolerences, ε.

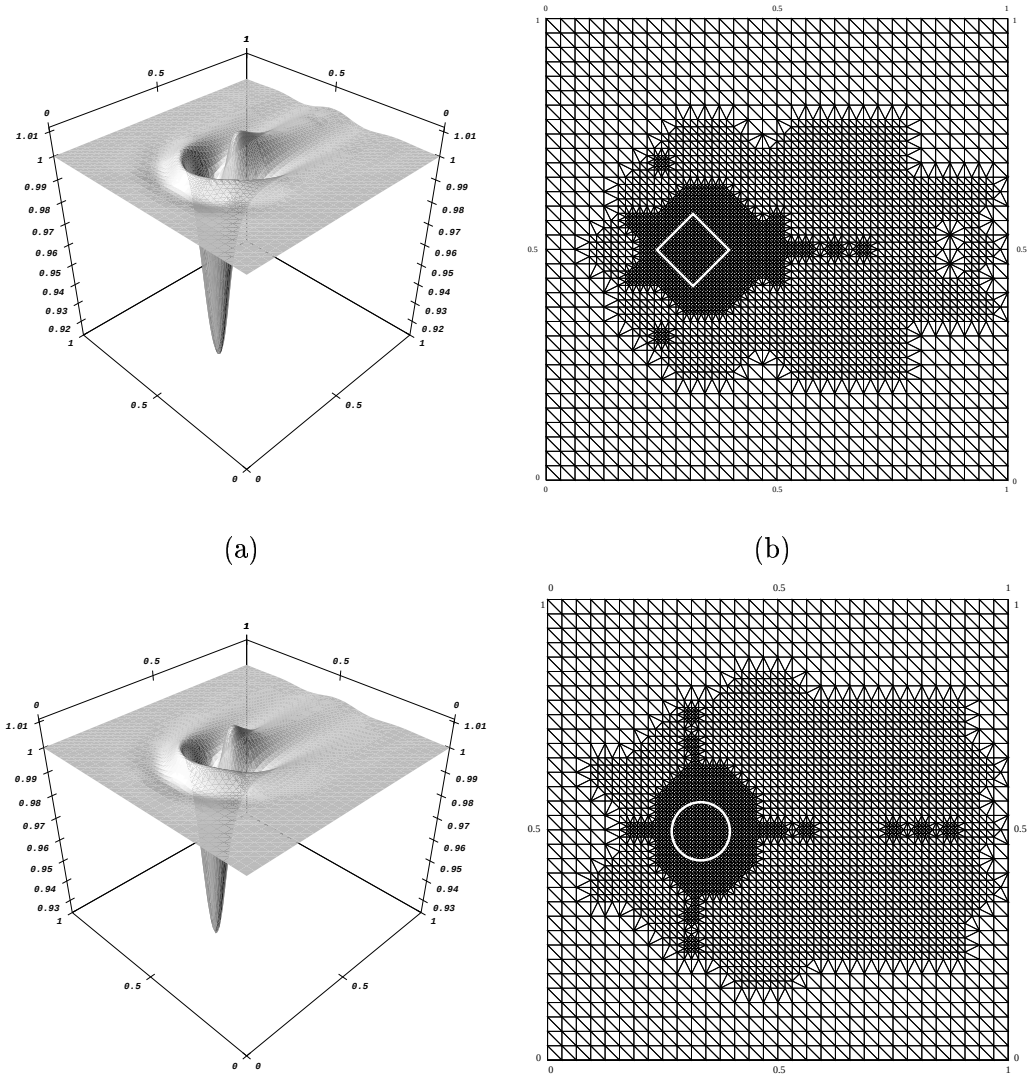

Fig. 11. Steady-state free-surface, $h+s$, profiles (left) and associated adaptive mesh distributions (right) for thin film flow over a diamond (top, $w_t = 0.1, s_0 = -0.1$) and cicular (bottom, $r_t = 0.05, s_0 = -0.1$) trench, using two levels of adaptive refinement with tolerence, $\varepsilon = 0.01\tau_k^{k-1}$.

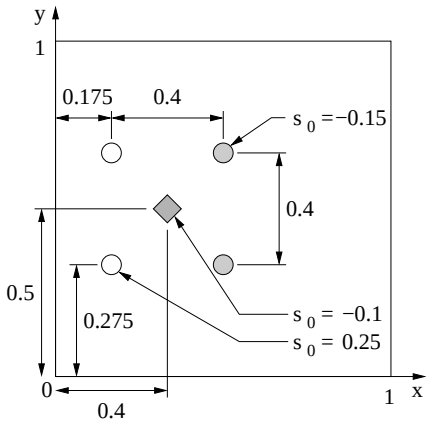

(a)

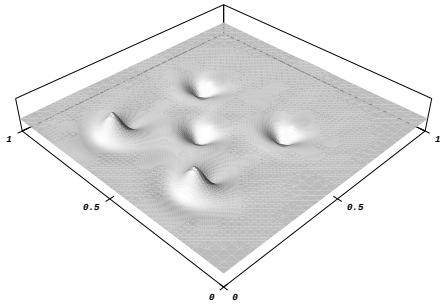

(b)

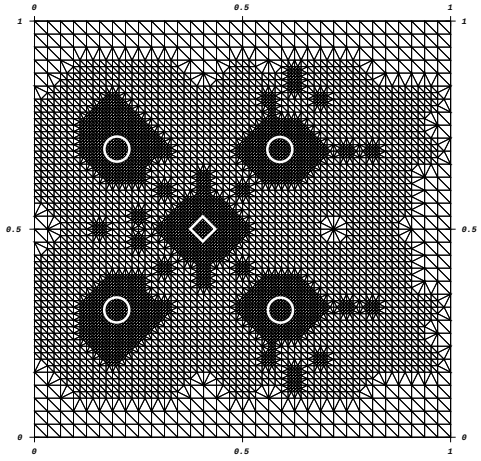

(c)

Fig. 12. Case 1: (a) Geometrical definition, (b) resulting steady-state free surface profile, and (c) corresponding adaptive mesh distribution, showing the combined effects of surrounding a diamond shaped trench topography ($w_t = 0.05, s_0 = -0.1$), with a distribution of circular peaks, $s_0 = 0.25, r_t = 0.025$ (upstream), and circular trenches, $s_0 = -0.15, r_t = 0.025$ (downstream), for $\varepsilon = 0.05\tau_k^{k-1}$ on uniform coarse grid $k = 2$ with 2 local refinement levels.

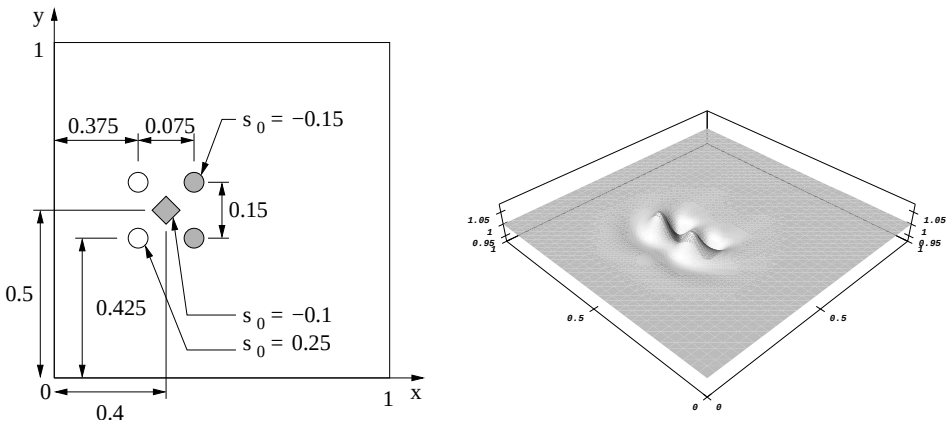

(a)

(b)

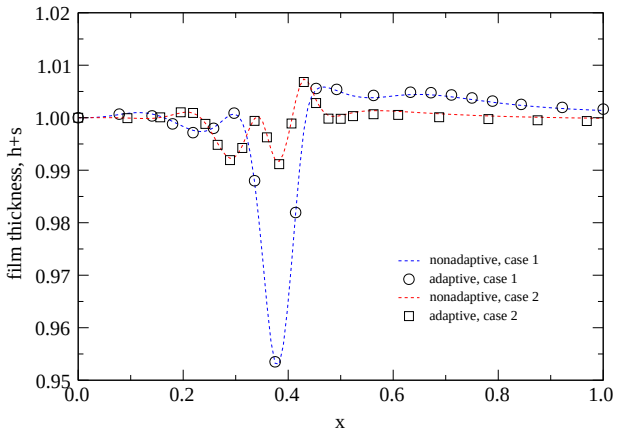

(c)

Fig. 13. Case 2: (a) Re-distribution of topography defined in Figure 12(a), and (b) its resulting free surface profile, illustrating (c) the reduction in planarisation disturbances along the streamwise, $y = 0.5$, direction; solutions obtained adaptively ($\varepsilon = 0.05\tau_k^{k-1}$ on a uniform coarse grid $k = 2$ with 2 local refinement levels) and non-adaptively (fine grid, $k = 4$).

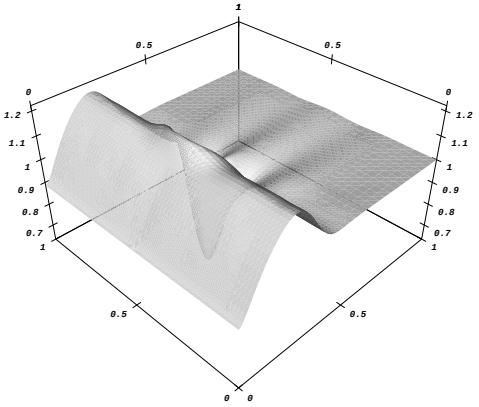

(a) $t = 0.15$.

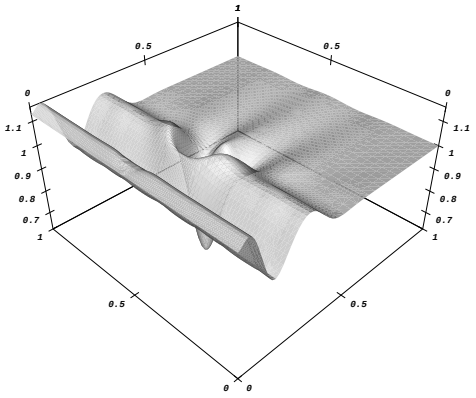

(b) $t = 0.15$.

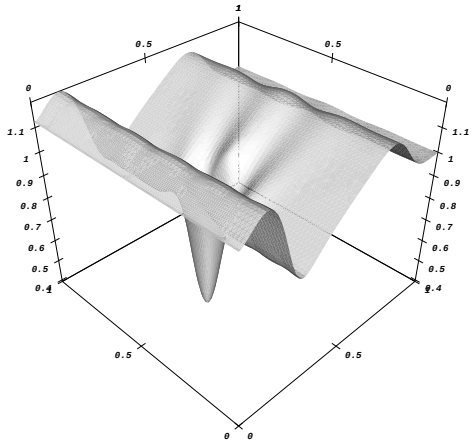

(c) $t = 0.35$.

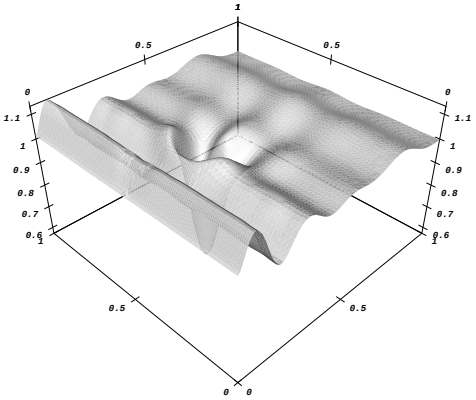

(d) $t = 0.35$.

Fig. 14. Free surface profiles for film flow over a square trench topography ($w_t = 0.1, s_0 = -0.5$) at different times, for the case of a sinusoidally varying inlet film thickness of frequency $f = 4Hz$ (left) and $f = 10Hz$ (right). Solutions obtained adaptively are presented on global coarse grid, $k = 2$, with three levels of local refinement and tolerence, $\varepsilon = 0.05\tau_k^{k-1}$.

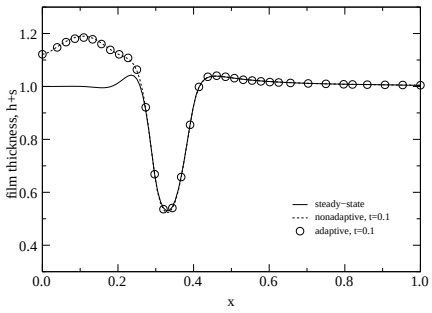

(a) $t = 0.1$.

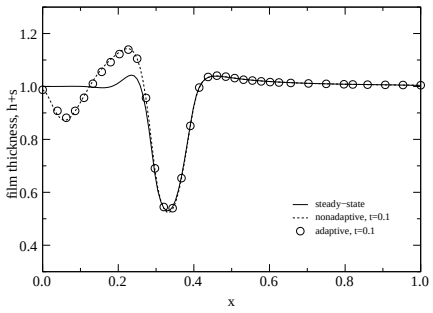

(b) $t = 0.1$.

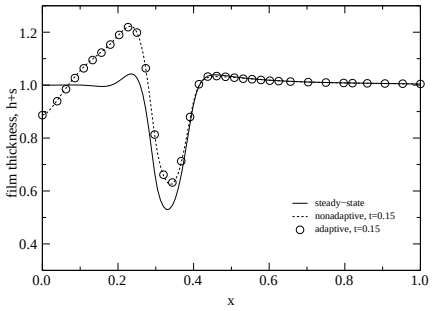

(c) $t = 0.15$.

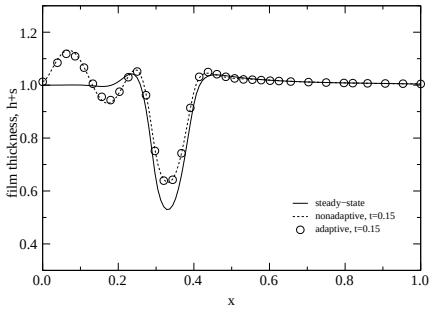

(d) $t = 0.15$.

Fig. 15. Evolving streamwise, $y = 0.5$, free surface profiles for the variable inlet flow problem, with sinusoidal frequency, $f = 4\,Hz$ (left) and $f = 10\,Hz$ (right), for flow over a square trench topography ($w_t = 0.1, s_0 = -0.5$). Solutions obtained adaptively (global coarse grid, $k = 2$, with three levels of local refinement, $\varepsilon = 0.05\tau_k^{k-1}$) and non-adaptively (fine grid, $k = 5$) are super-imposed against the steady-state solution, depicting formation of surge humps downstream of the topography.

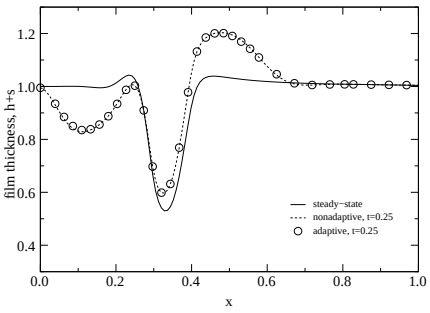

(e) $t = 0.25$.

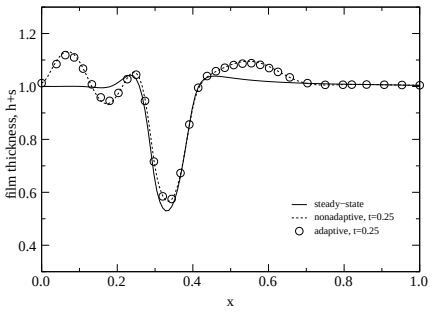

(f) $t = 0.25$.

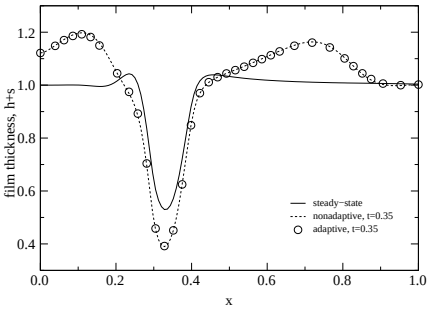

(g) $t = 0.35$.

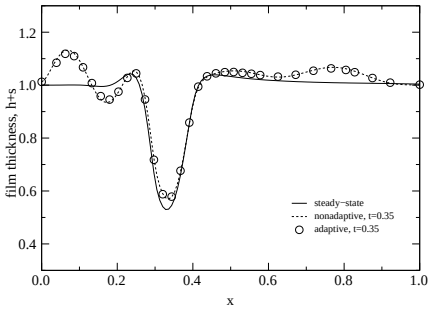

(h) $t = 0.35$.

Fig. 15. (continued).